The influence of local electronic character and nonadiabaticity in the photodissociation of nitric acid at 193 nm

T. L. Myers, N. R. Forde, B. Hu, D. C. Kitchen, and L. J. Butler
The James Franck Institute and Department of Chemistry, The University of Chicago, Chicago, Illinois 60637

(Received 10 February 1997; accepted 8 July 1997)

The dissociation of nitric acid upon $\pi_{nb,\mathrm{O}} \rightarrow \pi^*_{\mathrm{NO_2}}$ excitation at 193 nm has been studied in a crossed laser-molecular beam apparatus. The primary reaction channels are $\mathrm{OH}+\mathrm{NO_2}$ and $\mathrm{O}+\mathrm{HONO}$. We measure the branching ratio between these two competing processes and determine $(\mathrm{OH}+\mathrm{NO_2})/(\mathrm{O}+\mathrm{HONO})=0.50\pm0.05$. Our experiments provide evidence of a minor $\mathrm{O}+\mathrm{HONO}$ pathway, which we assign to $\mathrm{O}(^3P)$ and HONO in its lowest triplet state. The dominant pathway correlates to $\mathrm{O}(^1D)+\mathrm{HONO}(X\ ^1A')$. The translational energy distributions reveal two distinct pathways for the $\mathrm{OH}+\mathrm{NO_2}$ channel. One pathway produces stable $\mathrm{NO_2}$ fragments in the $1\,^2B_2$ electronic state. The second pathway produces unstable $\mathrm{NO_2}$ fragments which undergo secondary dissociation to $\mathrm{NO}+\mathrm{O}$. We examine the influence of nonadiabaticity along the $\mathrm{OH}+\mathrm{NO_2}$ reaction coordinate in order to explain the significant branching to this other channel. Finally, we introduce a new method for generating correlation diagrams for systems with electronic transitions localized on one moiety, in which we restrict the changes allowed in remote molecular orbitals along the reaction coordinate. Analysis of previously measured $X+\mathrm{NO_2}$ photofragment pathways in nitromethane and methyl nitrate provides further support for using a restricted correlation diagram to predict the adiabatic and nonadiabatic product channels. © *1997 American Institute of Physics.* [S0021-9606(97)01638-3]

I. INTRODUCTION

While the bulk of this paper seeks to investigate the specific competing adiabatic and nonadiabatic dissociation channels of nitric acid at 193 nm, two results in the paper address broader issues. First, the adiabatic $\mathrm{OH}+\mathrm{NO_2}(1\,^2B_2)$ reaction pathway, which is one of the two $\mathrm{OH}+\mathrm{NO_2}$ channels experimentally observed, belongs to a general class of reactions where the individual orbital symmetry is not conserved along the reaction coordinate. Thus, this system provides the opportunity to test whether such reactions are particularly susceptible to electronically nonadiabatic effects. Second, the analysis of our results on nitric acid suggests an approach to determine what product channels are inaccessible when nonadiabatic effects play an important role. We find in nitric acid that product channels which require the OH radical orbital to change symmetry from a' in the reactant region to a'' in the product region, with a complementary change in the occupied $\mathrm{NO_2}$ orbitals necessary to maintain the overall state symmetry, simply are not observed experimentally. Such a change in the electronic wave function during reaction is evidently even more difficult for a molecule to accomplish than a switch in the individual orbital symmetry when both sets of orbitals are localized on the same moiety. Thus, we introduce a ''restricted adiabatic'' correlation diagram that disallows correlations to product channels when such drastic changes in the electronic wave function are required. In the specific, but not narrow, class of systems in which the relevant molecular orbitals are effectively localized in both the reactants and products, such restricted correlation diagrams should prove useful in identifying which reaction channels are viable ones. The potential significance to any reactive system with electronically localized functional groups is clear.

Many research groups have investigated the photodissociation of nitric acid in the ultraviolet region due to its importance in atmospheric chemistry. Although these studies indicate the major primary products from the photodissociation of nitric acid at 193 nm are $\mathrm{OH}+\mathrm{NO_2}$ and $\mathrm{O}+\mathrm{HONO}$,[1–3] the quantum yields of these products remain disputed. Furthermore, the role of electronic nonadiabaticity in the dissociation dynamics of the competing channels and the identity of the $\mathrm{NO_2}$ products have not been elucidated. We begin with a brief review of the relevant experimental and theoretical work on nitric acid before presenting our goals for this paper.

The broad and structureless ultraviolet absorption spectrum[4] for nitric acid results from three transitions involving orbitals localized on the $\mathrm{NO_2}$ moiety. The intense absorption band with a maximum at 190 nm ($\sigma=10^{-17}$ cm^2) involves a $\pi_{nb,\mathrm{O}} \rightarrow \pi^*_{\mathrm{NO_2}}$ transition to the $2\,^1A'$ electronic state. At wavelengths longer than 200 nm in the absorption spectrum, the major primary process is production of $\mathrm{OH}+\mathrm{NO_2}$ (Ref. 5), and there have been several recent detailed studies of the OH photofragment angular distributions, lambda doublet ratios, and $v-J$ correlations,[6–9] as well as analysis of the fluorescence from the $\mathrm{NO_2}$ product.[10,11] Excitation to the $2\,^1A'$ excited state for nitric acid leads to both $\mathrm{OH}+\mathrm{NO_2}$ and $\mathrm{O}+\mathrm{HONO}$ products. Although the quantum yields for these products have been investigated, conflicting measurements have been reported. Ravishankara and co-workers[1] detect OH products via pulsed laser-induced

fluorescence and report $\Phi(\mathrm{OH})=0.33\pm0.06$. They also use atomic resonance fluorescence detection to determine the quantum yields for $\mathrm{O}[\mathrm{O}(^3P)+\mathrm{O}(^1D)]=0.81\pm0.13$ and $\mathrm{O}(^3P)=0.53\pm0.13$, which differ to give $\mathrm{O}(^1D)=0.28\pm0.07$, and they report a minor primary dissociation channel producing $\mathrm{H}+\mathrm{NO}_3$ with a quantum yield of $\leqslant0.012$. Schiffman and Nesbitt,[2] on the other hand, detect the OH fragment with high resolution infrared absorption spectroscopy and report a higher OH quantum yield, $\Phi(\mathrm{OH})=0.47\pm0.06$. A third group, Huber and co-workers,[3] use photofragment translational spectroscopy to determine the yield for $\mathrm{OH}+\mathrm{NO}_2$ to be $\Phi(\mathrm{OH})=0.6\pm0.1$ and for $\mathrm{O}+\mathrm{HONO}$ to be $\Phi(\mathrm{HONO})=0.4\pm0.1$.

More important than the conflicting branching ratios is that the electronic states of the products have not been correctly assigned. One difficulty is that prior experimentalists have interpreted their data using *ab initio* electronic structure calculations by Bai and Segal, the only *ab initio* calculations for nitric acid along the $\mathrm{OH}+\mathrm{NO}_2$ reaction coordinate.[12] Their results show the $1\,^1A''$ state correlating to $\mathrm{OH}+\mathrm{NO}_2(1\,^2A_1)$ and the $2\,^1A''$ and $2\,^1A'$ states correlating to $\mathrm{OH}+\mathrm{NO}_2(1\,^2B_1)$ at bent NO_2 geometries. The assignment for the $\mathrm{NO}_2(1\,^2B_1)$ state, however, is incorrect. They claimed the $1\,^2B_2$ state is linear and therefore energetically inaccessible at the highly bent geometry of NO_2 in nitric acid. In fact, it is the $1\,^2B_1$ state which is linear.[13] Thus, the $2\,^1A''$ and $2\,^1A'$ states should correlate to $\mathrm{OH}+\mathrm{NO}_2(1\,^2B_2)$ at bent geometries. Many authors have quoted Bai and Segal's work to interpret their experimental results; therefore, we correct the correlation diagrams in this paper before introducing a new method for generating a restricted correlation diagram to predict the observed nonadiabatic product channels.

Prior photofragment translational energy measurements by Huber and co-workers[3] revealed a bimodal translational energy distribution for the $\mathrm{OH}+\mathrm{NO}_2$ channel. They claimed correctly that one channel produces NO_2 fragments with enough internal energy to undergo secondary decay to $\mathrm{NO}+\mathrm{O}(^3P)$. They proposed, however, that the unstable NO_2 fragments may be either formed as electronically excited $\mathrm{NO}_2(1\,^2B_1)$ or ground state $\mathrm{NO}_2(1\,^2A_1)$. They also showed that the other channel produces stable NO_2 product since more of the available energy goes into translation. Due to the small fluorescence quantum yield of electronically excited NO_2 upon photodissociation of nitric acid at 193 nm,[14] they concluded that this second channel produces NO_2 in its ground electronic state $(^2A_1)$ via internal conversion to a lower electronic state. We will show in this paper that this assignment of the NO_2 product electronic states is incorrect.

Some disagreement concerning the electronic states of the $\mathrm{O}+\mathrm{HONO}$ products also exists. Stuhl and co-workers[15] used pump–probe experiments to record $\mathrm{OH}(A-X)$ emission from a two-photon process involving HONO, the intermediate produced from the photolysis of nitric acid at 193 nm. They observed rotational levels for OH up to $N'=31$ with ArF as the probe laser and up to $N'=19$ with KrF as the probe laser. Based on energetics and spin conservation, they proposed that HONO is formed in its lowest triplet state with $\mathrm{O}(^3P)$ as its coproduct. Ravishankara and co-workers[1] detected the formation of both $\mathrm{O}(^3P)$ and $\mathrm{O}(^1D)$, which suggests that both singlet and triplet HONO could be produced. Although some of the $\mathrm{O}(^3P)$ resulted from secondary dissociation of NO_2, the high quantum yield for $\mathrm{O}(^3P)$ indicates another source is also present. On the other hand, Huber and co-workers[3] propose that only singlet HONO and $\mathrm{O}(^1D)$ are produced at 193 nm. Our experiments presented here show that both channels occur.

In this paper, we measure the photofragment velocity and angular distributions in a crossed laser-molecular beam apparatus to investigate the primary reaction pathways in nitric acid excited at 193 nm. We measure the branching ratio between the $\mathrm{OH}+\mathrm{NO}_2$ and the $\mathrm{O}+\mathrm{HONO}$ channels. Using our translational energy distributions, we identify the electronic states of the photofragments. To provide further support for our assignments, we present adiabatic correlation diagrams along the $\mathrm{OH}+\mathrm{NO}_2$ and the $\mathrm{O}+\mathrm{HONO}$ reaction coordinates. We also examine the influence of nonadiabatic effects along the $\mathrm{OH}+\mathrm{NO}_2$ reaction coordinate and develop a restricted correlation diagram which we use to predict the major product channels that occur in nitric acid as well as similar systems such as methyl nitrate and nitromethane.

II. EXPERIMENT

A. Molecular beam experiments

We use a crossed laser-molecular beam apparatus with a rotatable molecular beam source[16,17] to measure the photofragment time-of-flight (TOF) distributions from the dissociation of nitric acid. After thoroughly degassing the nitric acid, we bubbled helium through the liquid sample of 90% nitric acid maintained at 10 °C. This 4% gaseous mixture of nitric acid (96% He)[18] was expanded through a 0.10 mm diameter nozzle at a total stagnation pressure of 300 Torr generating the molecular beam. To reduce the formation of clusters during the supersonic expansion, we heated the nozzle to 104 °C. (We took a helium beam TOF to determine the nozzle temperature.) The velocity distribution of the parent molecular beam is measured by rotating the source so that it points directly into the detector and raising a chopper wheel into the beam.

We use a Lumonics PM-848 pulsed excimer laser to produce the 193 nm light. The unpolarized laser light was focused to a 6 mm^2 spot size in the interaction region. The power, measured with a Scientech 362 power energy meter, was approximately 7 mJ/pulse in the interaction region. The neutral dissociation products formed at the crossing point of the laser and molecular beams travel 44.13 cm to an electron bombardment ionizer where ionization is induced by 200 eV electrons. The resulting ions are then mass-selected with a quadrupole mass filter and counted with a Daly detector. The signal intensity of the mass-selected fragment with respect to its time-of-arrival is recorded with a multichannel scaler.

The angular distributions of the photofragments are obtained by polarizing the laser beam and measuring the change in signal intensity with the laser polarization angle. The laser beam is polarized by a single crystal quartz Pellin-

Broca, which disperses the unpolarized light into two linearly polarized components. The horizontal component is utilized, and the polarization is rotated with a half-wave retarder. We calibrate the half-wave retarder by placing another Pellin-Broca after the half-wave plate and rotating the half-wave plate until the vertical component disappears, corresponding to a laboratory polarization angle of 90°. The polarized laser light was focused to a 3 mm^2 spot size, and the measured power was approximately 3 mJ/pulse in the interaction region. Laser polarization angles and molecular beam source angles are defined with respect to the detector axis as positive with counterclockwise rotation, and positive with clockwise rotation, respectively.

We observed signal for $m/e^+=46$, NO_2^+, at source angles of 10 and 15°, for $m/e^+=17$, OH^+, at 6, 8, 10, 30, and 35°, for $m/e^+=30$, NO^+, at 6, 10, and 20°, and for $m/e^+=16$, O^+, at 10°. We definitively identify any signal resulting from clusters in the supersonic expansion by taking data at the parent mass, HNO_3^+, at 6°. We observed a very small peak at HNO_3^+ after 1 million shots due to clusters in the beam. We fit this signal with a velocity distribution, which we use to identify contributions from clusters for the other masses at small angles. We did not observe any evidence for O–H bond fission since no signal was seen for $m/e^+=62$, NO_3^+, at 10° after 1 million shots. We did not look for signal at the momentum-matched fragment, H^+, since H has a poor ionization cross section, and the ambient background at this mass is high, making the detection of H atoms with a mass spectrometer difficult.

B. Branching ratios

Prior molecular beam experiments by Huber and coworkers used their integrated signal intensities at OH^+ to determine the branching ratio between $OH+NO_2$ and O+HONO. Thus, they had to correct their branching ratio for the fraction of HONO radicals which ionize to give OH^+. In their calculation of the HONO fragmentation pattern, they only considered OH^+, NO^+, and NO_2^+ as significant daughter ions; however, contributions from other fragments, especially O^+, may not be minimal. To avoid using the daughter-ion cracking pattern of HONO in our branching ratio calculation, we integrate the signal for the O+HONO channel at O^+ corresponding to the signal from the O atom fragment, the momentum-matched partner to HONO, and for the $OH+NO_2$ channels at OH^+.

For the branching ratio data, the source angle was maintained at 10° with respect to the detector axis. In order to average out systematic errors, including fluctuations in the parent molecular beam, we alternated between OH^+ and O^+. Each scan for $m/e^+=17$, OH^+, was collected for 10 000 shots, whereas each scan for $m/e^+=16$, O^+, was collected for 50 000 shots. The laser beam was stabilized to 7 mJ/pulse in the interaction region and operated at 150 Hz. To test the validity of our branching ratio, we repeated these experiments three times. The first set of data was collected over 34 scans for each mass, the second set was collected over 30 scans each, and the last set was collected over 42 scans each.

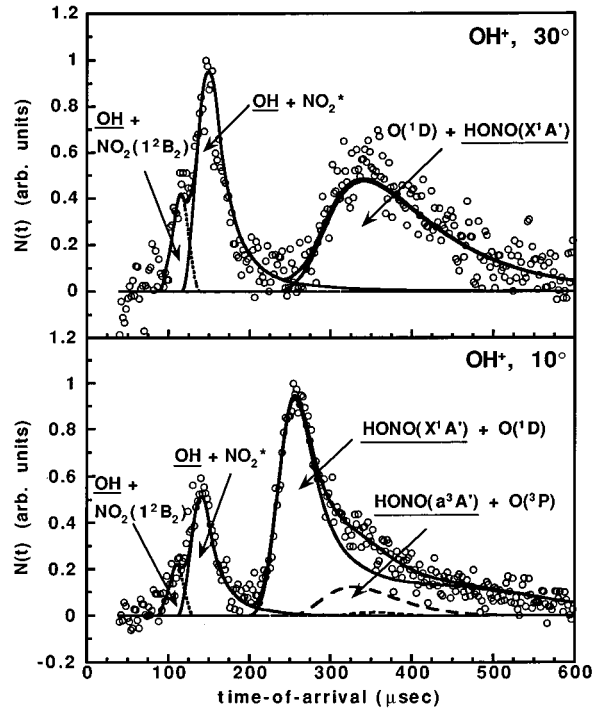

FIG. 1. The top frame shows the laboratory TOF spectrum of the photofragments detected at OH^+ with a source angle of 30° after 750 000 laser shots. The fast peak results from two $OH+NO_2$ channels and is fit with the $P(E_T)$s presented in Fig. 7. We represent the NO_2 electronic state that we are unable to identify by NO_2^*, which represents a higher electronic state than $NO_2(1\,^2B_2)$. The slow signal results from O+HONO and is fit with the faster $P(E_T)$ in Fig. 6. The bottom frame shows the laboratory TOF spectrum of the photofragments detected at OH^+ with a source angle of 10°. This TOF reveals another O+HONO channel at low kinetic energies. This signal is fit with the slower $P(E_T)$ in Fig. 6. This TOF is also used in the branching ratio calculation in which the signal for the $OH+NO_2$ channels is integrated from 94–190 μs.

Quadrupole resolution was maintained at 1.0 amu full width at half maximum (FWHM) for all three sets. The beam had an average peak velocity of 1.36×10^3 m/s and a FWHM of 11.5%. Although we only present the data for the branching ratio from the final set, we calculate the branching ratio from the average of all three sets, and our reported error represents a 95% confidence limit in the mean.

III. RESULTS AND ANALYSIS

A. Identification of primary product channels

The TOF spectrum shown in the top frame of Fig. 1 for OH^+ at 30° is evidence for three of the competing channels, two pathways for $OH+NO_2$ formation and one for O+HONO formation (HONO cracks in the ionizer to give OH^+). The bottom frame of Fig. 1 shows the TOF spectrum of OH^+ at 10°. This spectrum includes a second O+HONO channel, which we identify in the following manner. In order to determine if clusters contributed to this signal, we fit the HNO_3^+ TOF in the top frame of Fig. 2. The corresponding velocity distribution in the bottom frame of Fig. 2, however, shows the clusters are recoiling too slowly to appear signifi-

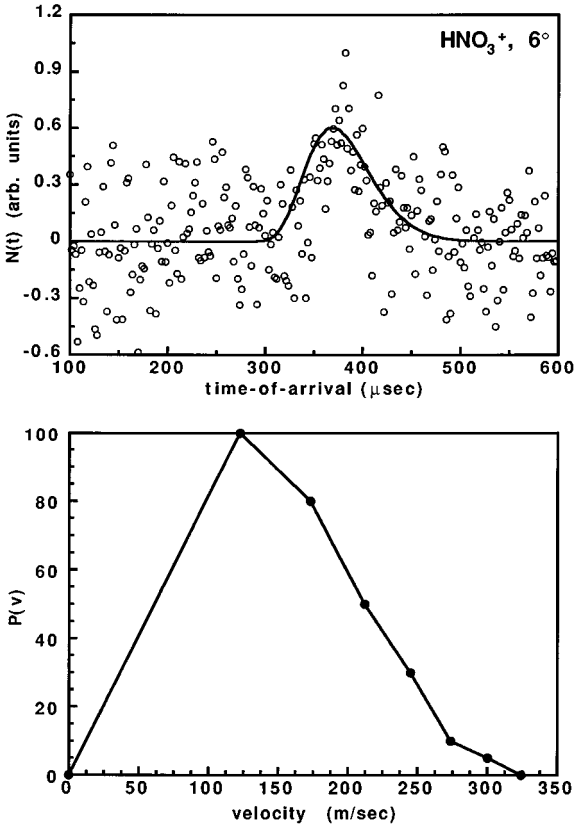

FIG. 2. The top frame shows the laboratory TOF spectrum of the photofragments detected at HNO_3^+ with a source angle of 6° after 1 million laser shots. Since the signal occurs at the parent mass, it must result from clusters present in the supersonic expansion. The bottom frame shows the center-of-mass velocity distribution of the photofragments from cluster dissociation. It is derived from forward convolution fitting the HNO_3^+ signal above. The maximum angle of detection for clusters traveling at a velocity of 200 m/s with a parent beam velocity of 1260 m/s is 9°; therefore, this signal is too slow to show up at 15°.

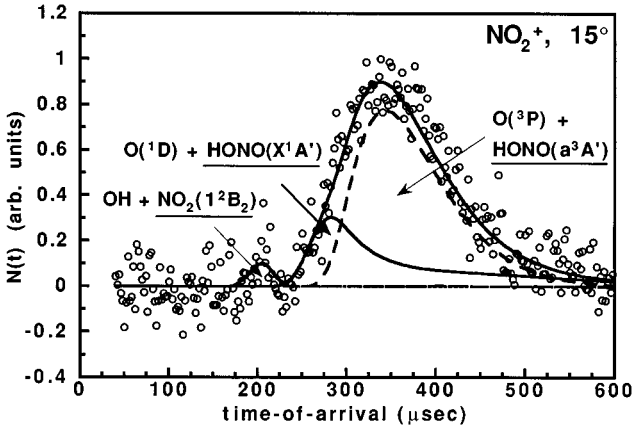

FIG. 3. Laboratory TOF spectrum of the photofragments detected at NO_2^+ with a source angle of 15° after 1 million laser shots. This spectrum clearly shows the second O+HONO pathway since the slow, broad signal in this TOF cannot be fit by any of the three channels evidenced at OH^+ at 30° in the top frame of Fig. 1. The signal is also too fast to result from clusters as indicated in Fig. 2, since the measured parent beam velocity was 1260 m/s. Note the very different cracking patterns of ^{3}HONO and ^{1}HONO; the former favors NO_2^+ while the latter is more easily detected at OH^+.

cantly at 10°. Thus, another channel must be contributing to the OH^+ signal. This slow signal also appears in the TOF spectrum for NO_2^+ at 15°, Fig. 3, and NO^+ at 10°, Fig. 4. By attributing this signal at OH^+ and NO_2^+ to daughter ions of HONO from a second O+HONO channel, we can also fit its momentum-matched partner, O, in the O^+ TOF spectrum, Fig. 5. In the O^+ TOF, we also see signal resulting from the parent HONO cracking in the ionizer to O^+. The HONO fragments from the two pathways, however, possess very different cracking patterns, which can be easily seen by comparing the OH^+ and NO_2^+ TOFs. The vastly different cracking patterns suggest the HONO fragments are in different electronic states.[19] We can adequately fit all our data for OH^+, O^+, and NO_2^+ from these four primary reaction pathways. The signal in the NO^+ TOF spectrum that is not fit results from the secondary dissociation of NO_2.

The translational energy distributions, $P(E_T)_s$, used to fit the two O+HONO channels, are shown in Fig. 6. We estimate the competition between the two O+HONO pathways from the relative probabilities of the O atom fragments, the momentum-matched partners to HONO, used to fit the O^+ TOF in Fig. 5. The branching ratio between the fast and slow O+HONO channels is 4:1; therefore, the slower O+HONO channel is only a minor process. The kinetic energy distributions used to fit the two $OH+NO_2$ channels shown in Fig. 7 are in agreement with those reported by Huber and co-workers.[3] One channel produces stable fragments with an average translational energy of 39 kcal/mol. The other channel produces fragments with an average translational energy of 16 kcal/mol, so that the NO_2 fragments have enough internal energy to undergo secondary dissociation to $NO+O(^3P)$, as previously proposed by both Huber and co-workers and Chen and co-workers.[20] This is also reflected in our NO_2^+ TOF, where this second $OH+NO_2$ channel does not appear. We determine the branching ratio between the fast and slow $OH+NO_2$ channels of 1.0:2.2 from

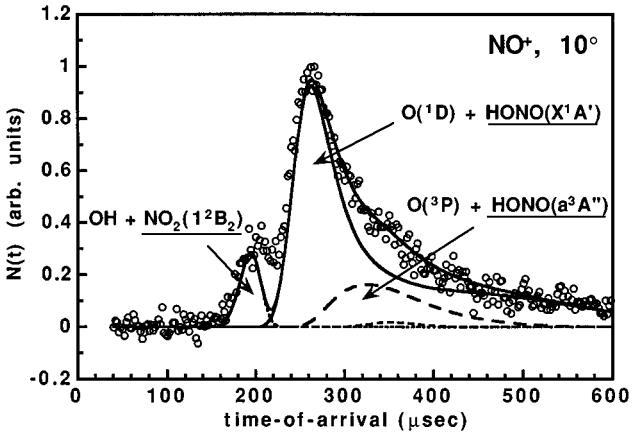

FIG. 4. Laboratory TOF spectrum of the photofragments detected at NO^+ with a source angle of 10° after 200 000 laser shots. The signal that is not fit is due to NO from the secondary dissociation of NO_2.

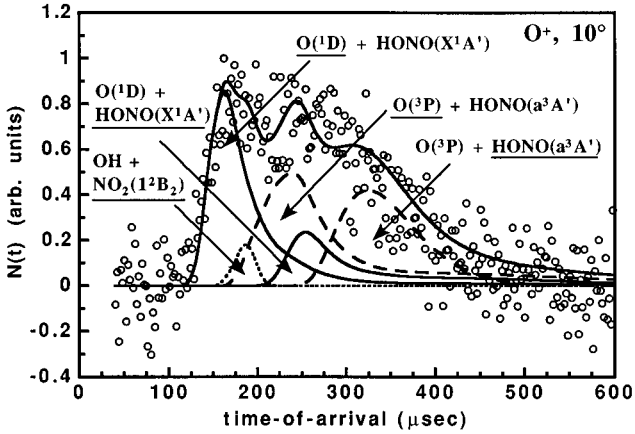

FIG. 5. Laboratory TOF spectrum of the photofragments detected at O^+. This signal shows the momentum-matched O atom fragments from both O+HONO channels. It also is fit with contributions from HONO cracking in the ionizer to give O^+ for both channels. This TOF is used for the branching ratio calculation in which the signal for the fast O+HONO channel is integrated over 130–150 μs to avoid any overlapping signal from other channels.

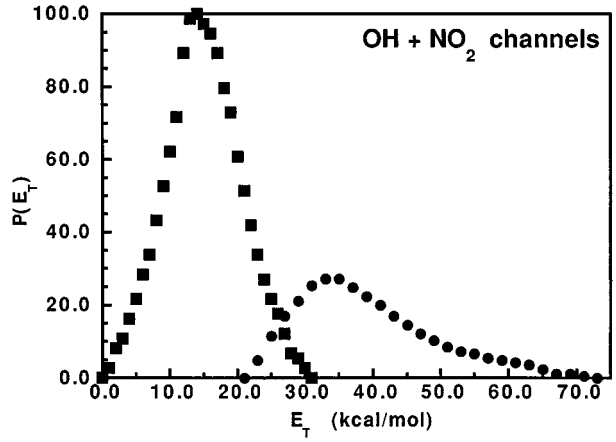

FIG. 7. Center-of-mass product translational energy distribution, $P(E_T)$, for $HONO_2 \rightarrow OH+NO_2$. The two distributions are derived from forward convolution fitting the first peak in the OH^+ TOF in Fig. 1. The branching ratio between the slow and fast $OH+NO_2$ channels is 2.2:1.0. The faster $P(E_T)$, which peaks at 35 kcal/mol, is assigned to $OH+NO_2(1\,^2B_2)$. The slower translational energy distribution, which peaks at 15 kcal/mol, corresponds to NO_2 fragments with enough internal energy to undergo secondary dissociation. The normalized $P(E_T)$s are scaled according to the relative probabilities used to fit the OH^+ data in Fig. 1.

the relative probabilities used to fit the OH^+ TOF. In the discussion, we assign the faster $OH+NO_2$ channel to $OH+NO_2(1\,^2B_2)$, which differs from that proposed by Huber.

B. Angular distributions

We fit our angular distribution measurements by varying the anisotropy parameter β in this expression for the intensity of the angular distribution of the fragments[21]

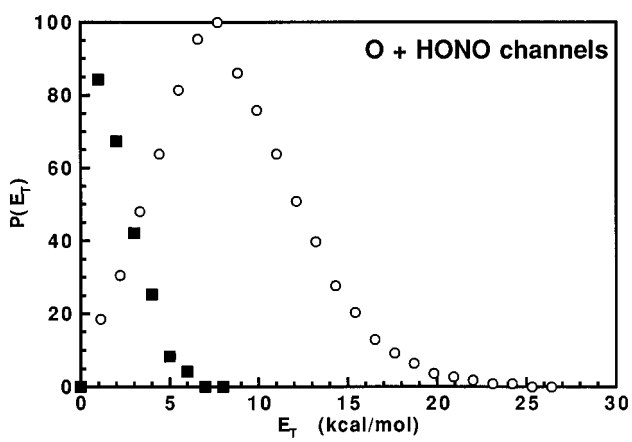

FIG. 6. Center-of-mass product translational energy distributions, $P(E_T)$s, for the $HONO_2 \rightarrow O+HONO$ channels. The fast component is derived from forward convolution fitting the OH^+ signal which peaks around 325 μs in the top frame of Fig. 1. This $P(E_T)$ is assigned to the formation of $O(^1D)+HONO(X\,^1A')$. The slow component is derived from forward convolution fitting the slow NO_2^+ signal, Fig. 3, which could not be fit from the other three channels. We assign this channel to $O(^3P)+HONO(a\,^3A'')$. The branching ratio between the fast and slow O+HONO channels is 4:1; therefore, the slow channel is only a minor pathway. The normalized $P(E_T)$s are scaled according to the relative probabilities used to fit the O^+ data in Fig. 5.

$$I(\theta_{\text{c.m.}}) = \frac{1}{4\pi}[1+\beta P_2(\cos\,\theta_{\text{c.m.}})], \tag{1}$$

in which $\theta_{\text{c.m.}}$ is the angle between the electric vector and the recoiling fragment in the center-of-mass reference frame. In the limit of prompt and axial recoil, the anisotropy parameter β can be expressed as[21]

$$\beta = 2P_2(\cos\,\alpha), \tag{2}$$

in which α is the angle between the transition dipole moment and the recoiling fragment. Since the photofragment angular distribution is measured in the laboratory frame, fitting the data involves converting between the center-of-mass and laboratory frames using the measured molecular beam velocity and the $P(E_T)$ determined from the unpolarized data.

Figure 8 shows the integrated HONO fragment signal from the O+HONO channel at OH^+ versus Θ_{LAB}, the angle between the electric vector of the polarized laser and the detector axis. The data are fit best with an anisotropy parameter, $\beta = +1.4$, which is more anisotropic than the value of $+0.6$ reported by Huber and co-workers. Their data may have included contributions from clusters which smear out the angular distribution. Our measured value is plausible, for if we assume that distortion of the molecule upon photoexcitation does not alter the recoiling bond direction before dissociation, and that the transition dipole moment is parallel to the terminal O atoms, the predicted $\beta = 2P_2(\cos 23.93°) = 1.5$ (Ref. 22).

Our angular distributions for the $OH+NO_2$ channels agree with Huber and co-workers. Figure 9 shows the integrated OH fragment signal from the $OH+NO_2$ channels at OH^+ versus Θ_{LAB}. The data for the slow $OH+NO_2$ fragment channel are fit best with $\beta = -0.6$, and the data for the fast $OH+NO_2$ fragment channel are fit best with $\beta = -0.5$.

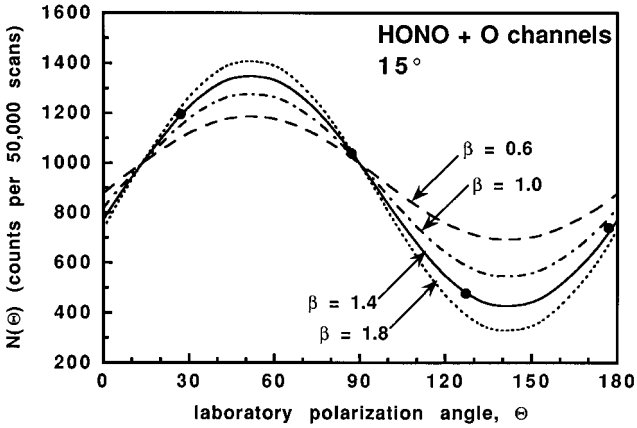

FIG. 8. Laboratory angular distributions of the HONO product measured at OH^+, which results from HONO cracking in the ionizer, with a linearly polarized laser and a source angle of 15°. The data points represent the integrated experimental TOF signal between 230–400 μs measured at four different laser polarization angles. Line fits show the predicted change in integrated signal with polarization angle using the same anisotropy parameter, β, for both channels and the $P(E_T)$s in Fig. 6, which are scaled according to the relative probabilities used to fit the two O+HONO channels in the OH^+ TOF in Fig. 1. The best fit is obtained with the solid line, which corresponds to $\beta=1.4$.

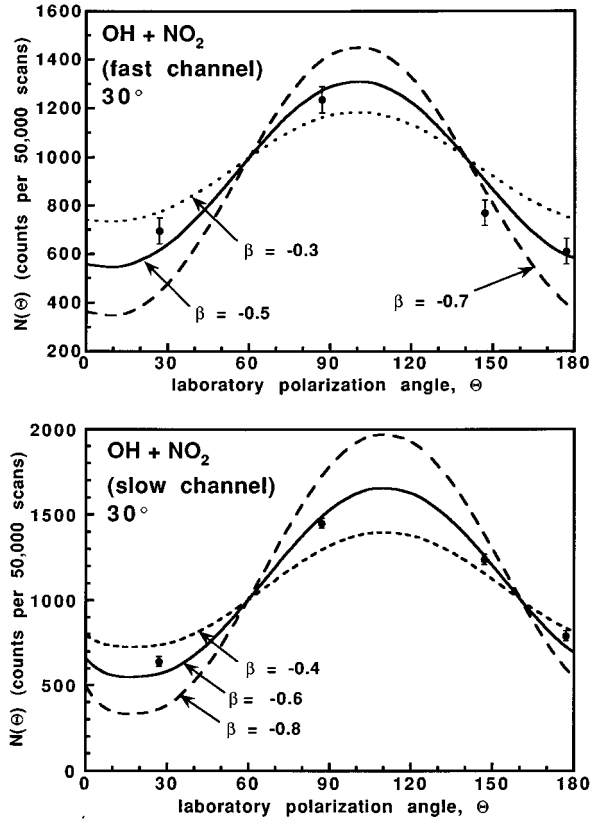

FIG. 9. The top frame shows the laboratory angular distributions of the faster OH product measured at OH^+ with a linearly polarized laser and a source angle of 30°. The data points represent the integrated experimental TOF signal between 102 and 114 μs measured at four different laser polarization angles. Line fits show the predicted change in integrated signal with polarization angle given an anisotropy β and the faster $P(E_T)$ in Fig. 7. The best fit is obtained with the solid line, which corresponds to $\beta=-0.5$. The bottom frame shows the laboratory angular distributions of the slow OH product measured at OH^+ with a linearly polarized laser and a source angle of 30°. The data points represent the integrated experimental TOF signal between 150 and 200 μs measured at four different laser polarization angles. Line fits show the predicted change in integrated signal with polarization angle given an anisotropy β and the slower $P(E_T)$ in Fig. 7. The best fit is obtained with the solid line, which corresponds to $\beta=-0.6$.

C. Branching ratio measurements

We calculated the branching ratio from the observed signals at O^+ (Fig. 5) and OH^+ (bottom frame of Fig. 1) and corrected for the ionization cross sections and kinematic factors. We integrated the signal for OH^+ over channels 47–95 (94–190 μs), subtracting the background from channels 8–40 (16–80 μs). For O^+, we integrated the signal from channels 65–75 (130–150 μs), which avoids any overlapping signal from other processes, and subtracted the background from channels 8–40. We did not include the minor O+HONO channel in our first branching ratio calculation because this signal is completely overlapped by other processes. We estimate the ionization cross sections of OH and O from their polarizabilities[23] to be 25.6 and 14.2 Å^2, respectively. Our reported branching ratio is the average from three separate measurements,

$$N\left(\frac{\mathrm{OH}}{\mathrm{O_{major}}}\right)=0.62\pm0.06. \tag{3}$$

We can estimate the contribution from the minor O+HONO channel from the relative probabilities used to fit the O product for both channels from the O^+ TOF. The branching ratio between these two processes is 4:1, which already includes corrections for the kinematic factors. Thus, we calculate the total branching ratio as

$$N\left(\frac{\mathrm{OH}}{\mathrm{O_{total}}}\right)=0.50\pm0.05. \tag{4}$$

IV. DISCUSSION

A. OH+NO_2 channels

As presented in Sec. III A, the data show two different kinetic energy distributions for the OH+NO_2 pathway in agreement with Huber and co-workers.[3] In this section, we attempt to definitively determine the NO_2 electronic states for both channels, beginning with the pathway which produces the stable NO_2 fragments. Huber assigned this channel to NO_2 in its electronic ground state ($X\ ^2A_1$); we, however, propose a different assignment for this channel. We assign the NO_2 electronic states by comparing our measured translational energy distributions for the OH+NO_2 channels, Fig. 7, with the predicted maximum and most probable kinetic energies for the NO_2 fragments. Obvious candidates are the low-lying excited states of NO_2. We obtain the maximum available translational energy from the minimum energies of the excited electronic states of NO_2 (Ref. 24) and the 47.6

TABLE I. Predicted most probable and maximum allowed kinetic energies for $OH+NO_2(Y)$.

State (Y)	ΔE_{vert} (eV)	E_{mp}^{trans} (kcal/mol)	ΔE_{min} (eV)	E_{max} (kcal/mol)
$1\,^2B_2$	2.78	34	1.18	73
$1\,^2A_2$	2.96	30	1.84	58
$1\,^2B_1$	3.15	25	1.66	62

kcal/mol bond dissociation energy. Since little energy is partitioned into internal energy of the OH fragment,[25,26] the excess energy after dissociation must go into internal energy of NO_2 and relative translational energy, allowing us to calculate not only the maximum available kinetic energy but also the most probable kinetic energy for the NO_2 fragments. We thus predict the peak kinetic energy in our measured $P(E_T)$s by estimating the most probable internal energy of the NO_2 fragments from a Franck–Condon projection of the initial NO_2 geometry in nitric acid onto the NO_2 product states, noting the geometry changes are primarily in the angle bend. We also simply subtract the average internal energy of the OH fragment, 2.7 kcal/mol, as reported by Chen and co-workers.[20] Using the equilibrium ONO angle in nitric acid (130°)[22] and potential energy curves of NO_2 along the ONO bending coordinate from multireference single and double configuration interaction calculations,[27] we determine the most probable internal energy of the NO_2 products for the three lowest-lying doublet states of NO_2. The most probable and the maximum available kinetic energies predicted for the $OH+NO_2$ fragments in each of the three low-lying excited NO_2 electronic states are listed in Table I. For example, the most probable kinetic energy predicted for any $OH+NO_2(1\,^2B_2)$ fragments is 34 kcal/mol, and the maximum available energy is 73 kcal/mol. These predicted results for $NO_2(1\,^2B_2)$ closely match the measured kinetic energy distribution for the stable NO_2 fragments, which peaks at 35 and extends to 73 kcal/mol. Similar results for the most probable kinetic energy are also obtained using MRD-CI calculations by Hirsch and Buenker[28] with an ONO angle of 130° and N–O bond lengths of 1.23 Å. These calculations predict the most probable internal energy for the NO_2 fragments to be 62 kcal/mol, which results in a most probable kinetic energy of 36 kcal/mol, after subtracting the average internal energy of the OH fragment. Thus, we assign the stable NO_2 fragments to the $1\,^2B_2$ state. Our assignment does not conflict with the fluorescence measurements since the $1\,^2B_2$ state undergoes rapid internal conversion to high vibrational levels in the ground state.[29]

If we use the same argument as above to assign the electronic state of the slower NO_2 product that undergoes secondary dissociation, we do not find a match from any of the three low-lying doublet states in Table I with the translational energy distribution in Fig. 7 used to fit this reaction channel. The most probable translational energies predicted for the $1\,^2B_1$ and the $1\,^2A_2$ electronic states of NO_2 are 25 and 30 kcal/mol, respectively. Our measured $P(E_T)$, on the other hand, peaks at 15 and extends to 34 kcal/mol, indicating the NO_2 product is formed with more internal energy than is predicted for any of the three low-lying excited states of NO_2.

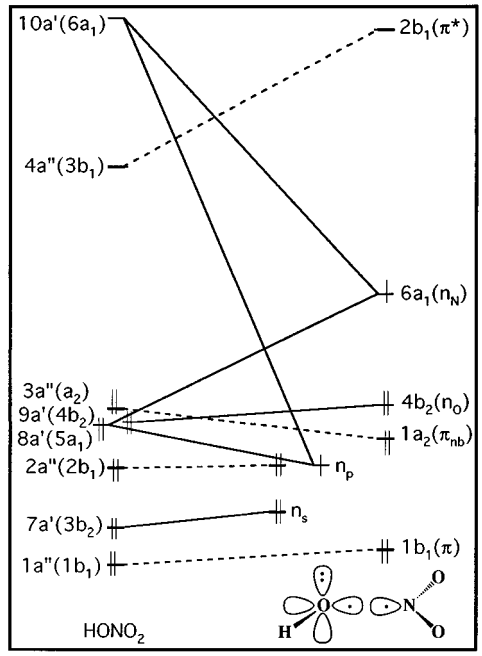

FIG. 10. Molecular orbital correlation diagram for the dissociation of nitric acid to $OH+NO_2$. The orbital energies for nitric acid are taken from Ref. 30. As noted in Ref. 30, the $2b_1$ orbital for nitric acid lies predominantly on the donor O fragment so that it correlates to the out-of-plane p orbital for the OH fragment. The sigma bonding and sigma antibonding orbitals of the N–OH bond in nitric acid $8a'(5a_1)$ and $10a'(6a_1)$, respectively, are taken as arising from the bonding and antibonding linear combinations of the OH n_p and the NO_2 $6a_1$ orbitals of the separated fragments. The orbital energies for the OH fragment are taken from Ref. 31. The orbital energies for NO_2 are taken from Refs. 32 and 33, and are calculated with a NO_2 bend angle of 134°, while that of nitric acid is 130°. The solid lines correspond to orbitals with a' symmetry whereas the dashed lines represent orbitals with a'' symmetry.

To help us determine the electronic state of this unstable NO_2 product and to further analyze our assignments, we generate a state correlation diagram along the $OH+NO_2$ reaction coordinate at bent NO_2 geometry. We first present a molecular orbital correlation diagram[30–33] in Fig. 10 for the fragmentation of nitric acid into $OH+NO_2$ products to illustrate the diabatic character of the reactant and product molecular orbitals. The usual adiabatic state correlation diagram shown in Fig. 11 assumes that every crossing between configuration states of the same symmetry is avoided and draws the correlation lines between the individual states of the reactants and products of equal symmetry. The barriers resulting from avoided crossings between states of similar symmetry are thus not shown, although you can easily determine them from the molecular orbital diagram in Fig. 10. The state correlation diagram illustrates that the $2\,^1A'$ excited state surface that is accessed at 193 nm correlates adiabatically to $NO_2(1\,^2B_2)$, which agrees with our assignment for the stable NO_2 product. This correlation diagram corrects the error by Bai and Segal,[12] which showed the $2\,^1A'$ state correlates

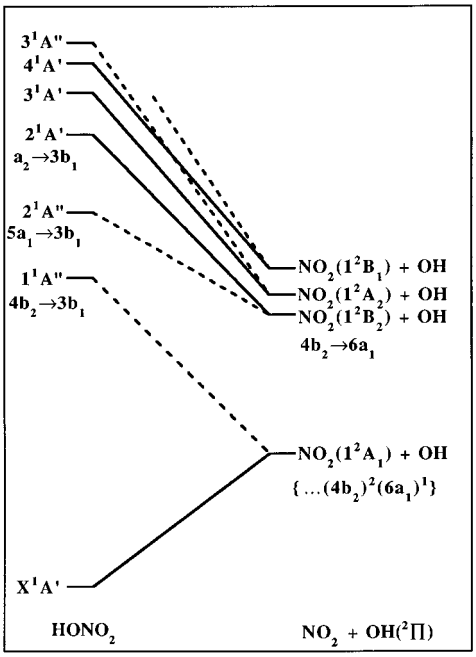

FIG. 11. Fully adiabatic state correlation diagram for the singlet states of nitric acid and the $OH+NO_2$ asymptotic products at bent NO_2 geometry. The vertical excitation energies for the excited states of nitric acid and for the NO_2 electronic states are taken from Ref. 22 and Ref. 37, respectively, and are calculated with a NO_2 bend angle of 130°. The $2\,^1A'$ state, which is accessed at 193 nm, correlates adiabatically to $OH+NO_2(1\,^2B_2)$. The A' states are indicated by the solid lines whereas the A'' states are indicated by the dashed lines. Each of the products correlates to both an A' and an A'' state because the OH radical p electron can be either a' or a'', as illustrated in Fig. 11. The unconnected line for the $NO_2(1\,^2B_1)+OH$ products correlates to the higher-lying $4\,^1A''$ excited state of nitric acid, which is not shown.

adiabatically to $NO_2(^2B_1)$. In order to understand why a second channel can compete with the adiabatic pathway for $OH+NO_2$, we consider the symmetries of the occupied NO_2 orbitals along the reaction coordinate. Since the individual orbital symmetry for NO_2 must change from $a''a''(a_2\rightarrow 3b_1)$ in the reactant to $a'a'(4b_2\rightarrow 6a_1)$ in the $NO_2(1\,^2B_2)$ product, this pathway is Woodward–Hoffman forbidden. Previous experiments[34] in our lab have illustrated that Woodward–Hoffmann forbidden reactions are particularly subject to a failure in the Born–Oppenheimer approximation. Thus, we expect the reaction dynamics to have difficulty traversing the adiabatic reaction coordinate. Since the reaction rate is reduced, other pathways can compete. In fact, the branching ratio between this second pathway and the adiabatic pathway which yields $NO_2(1\,^2B_2)$ is 2.2:1.0. This second pathway could result from a nonadiabatic hop to a nearby A' excited state in nitric acid. The correlation diagram in Fig. 11 gives two possible candidates, the $3\,^1A'$ and $4\,^1A'$ states, which correlate to $NO_2(1\,^2A_2)$ and $NO_2(1\,^2B_1)$, respectively. As we already stated, however, these two states are not responsible for this channel. In Sec. IV B, we propose a restricted correlation diagram to understand why neither the $NO_2(1\,^2B_1)$ or $NO_2(1\,^2A_2)$ products are formed.

We have considered other mechanisms for this channel. If we attempt to assign this channel to $O(^3P)+HONO(X\,^1A')$ and assume almost all of the 76.6 kcal/mol of available energy goes into internal energy of the HONO fragment, then HONO can undergo secondary dissociation to OH+NO, leaving 28.6 kcal/mol of available energy. If we assume all of the available energy goes into relative translation of the OH and NO products, we can fit the slow OH^+ signal peaking at 140 μs in the top frame of Fig. 1. Its momentum-matched signal at NO^+, however, overlaps the signal already attributed to the fast $OH+NO_2(1\,^2B_2)$ channel. It would not explain the signal that is not fit in the NO^+ TOF, Fig. 4. This signal is due to NO from the secondary dissociation of NO_2. [Although the NO_2 fragments from the fast $OH+NO_2(1\,^2B_2)$ channel with kinetic energies less than 28.7 kcal/mol have enough internal energy to undergo secondary dissociation, the contribution from these fragments is minimal and would not fit the NO^+ signal completely.] In addition, partitioning all 76.6 kcal/mol of the available energy into the HONO fragment, to produce such fast OH in this second channel, implies a negligible exit barrier for the O+HONO products; therefore, we do not believe this is a likely mechanism. If we instead assume all of the 76.6 kcal/mol of available energy goes into relative translation of the O+HONO fragments, then HONO does not have enough energy to undergo secondary dissociation, but would still crack in the ionizer to give the OH and NO fragments. This mechanism, however, is too slow to fit the OH^+ signal peaking at 140 μs in the top frame of Fig. 1. A third possibility that we have considered is a multiphoton process such as secondary photodissociation of HONO to OH+NO. Huber and co-workers[3] investigated the laser fluence dependence of the OH^+ signal. They observed at a high laser fluence of 500 mJ/cm^2, a decrease in the relative intensity of the peak for the HONO component with respect to the two peaks for the OH components. This decrease results from secondary photodissociation of HONO. The relative intensities between the two peaks for the $OH+NO_2$ channels, however, did not vary with laser power, suggesting that the slower of the two fast OH^+ peaks does not result from a secondary photodissociation process.

B. Restricted correlation diagram for the $OH+NO_2$ reaction coordinate

When both adiabatic and nonadiabatic product channels compete, as in nitric acid, the usual way of constructing an adiabatic correlation diagram can be useless in predicting what nonadiabatic channels might occur with high probability. For instance, the adiabatic correlation diagram in Fig. 11 would suggest that the A' states in proximity to the photoexcited $2\,^1A'$ state are the $3\,^1A'$ and $4\,^1A'$ states, so that a nonadiabatic hop to one of these states could occur, resulting in either $OH+NO_2(1\,^2A_2)$ or $OH+NO_2(1\,^2B_1)$ products. Yet, these experiments show that neither of the $OH+NO_2$ product channels resulting from these states are found. Clearly, assuming the molecule nonadiabatically hops from the $2\,^1A'$ state to a nearby A' state of nitric acid as depicted

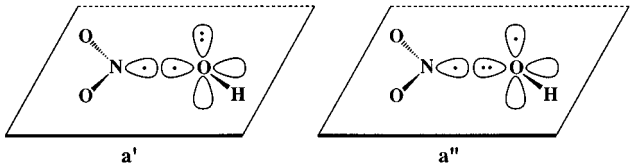

FIG. 12. Schematic which shows the radical p electron in OH can be either symmetric with respect to the molecular plane (a') or antisymmetric with respect to the molecular plane (a'').

in the full correlation diagram is not correct. In order to determine the identity of the observed nonadiabatic products, we need a better method for generating correlation diagrams.

To conceive of such a new correlation diagram, we considered the following. Because the electronic excitation is localized on the NO_2 moiety, and none of the energetically available NO_2 product states have the $\pi_{nb,O} \rightarrow \pi^*_{NO_2}$ character associated with the initial transition, a dissociation, whether adiabatic or nonadiabatic, must involve considerable electronic rearrangement. What if we generate a new ''restricted adiabatic'' correlation diagram which disallows any large changes in the electronic wave function on portions of the molecule remote from the NO_2 moiety? This is clearly not the usual way of constructing adiabatic correlation diagrams, yet it may provide us with a better picture of the reaction dynamics.

Since the OH fragment is remote from the NO_2 moiety, we propose that no large electronic changes in the OH fragment can occur during the dissociation. The full correlation diagram in Fig. 11 shows the asymptotic products correlating to both an A'' and an A' singlet state, which results because the OH fragment is doubly degenerate ($^2\Pi$): the lone p electron can either be in the plane of symmetry (a') defined by the plane of symmetry of the parent nitric acid molecule or perpendicular (a'') to it (Fig. 12). We propose that the radical p electron in the OH fragment remains in the plane of symmetry (a') as it is for the low-lying excited states of nitric acid. Our revised correlation diagram, presented in Fig. 13, restricts the radical p electron on OH to be in an a' orbital with respect to the parent plane of symmetry for the asymptotic products of all the low-lying excited states of nitric acid. All the correlations resulting from the radical p electron on the OH fragment being antisymmetric with respect to the molecular plane (a'') can, in our restricted diagram, only result from high-lying excited states of nitric acid [states where the σ^*(N–OH) orbital is occupied]. These are represented by light dotted lines in our figure. This correlation diagram still shows the restricted adiabatic pathway for the $2\,^1A'$ excited state leading to $OH+NO_2(1\,^2B_2)$; therefore, it does not conflict with our previous assignment.

This restricted adiabatic correlation diagram clearly demonstrates why the $NO_2(1\,^2A_2)$ and $NO_2(1\,^2B_1)$ asymptotic products of the $3\,^1A'$ and $4\,^1A'$ excited states of nitric acid in the fully adiabatic correlation diagram are not seen experimentally. These two product channels require the radical p electron on the OH moiety to change from being in the plane of the molecular system in the Franck–Condon

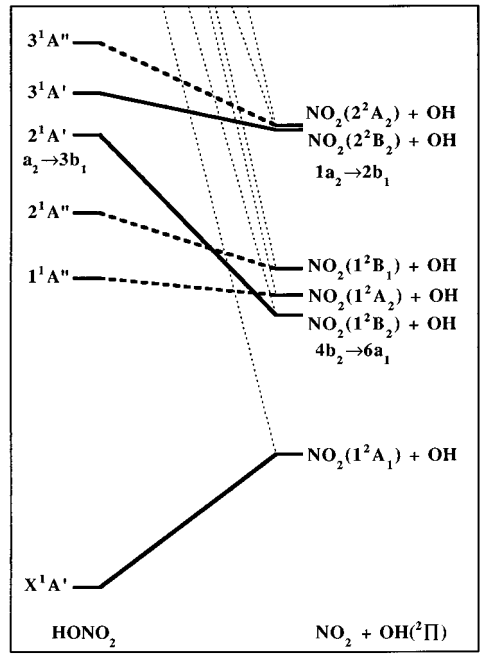

FIG. 13. ''Restricted adiabatic'' state correlation diagram for the singlet states of nitric acid and the $OH+NO_2$ asymptotic products with a NO_2 bend angle of 130°. The vertical excitation energies for the excited states of nitric acid and for the NO_2 electronic states are taken from Ref. 22 and Ref. 37, respectively. The bold dashed and solid lines correlate to products in which the OH radical p electron is restricted to remain symmetric with respect to the parent molecular plane of nitric acid, i.e., a'. The A' states are indicated by the solid lines whereas the A'' states are indicated by the dashed lines. The $2\,^1A'$ state, which is accessed at 193 nm, still correlates adiabatically to $OH+NO_2(1\,^2B_2)$. The light dotted lines represent states with electronic configurations in which the radical electron on the OH fragment occupies the p orbital perpendicular to the molecular plane (a'') in the asymptotic products and where a σ^*(N–OH) orbital is populated in the reactant region. These states are shown as basically decoupled from the states drawn with bold dashed and solid lines because the experimental results suggest the configuration interaction between them is negligible. Thus, dynamics beginning on the bold solid or dashed surfaces cannot cross to the dotted line surfaces. Therefore, the avoided crossings resulting from these configurations are not drawn, and the dotted lines are shown correlating to high-lying excited states of nitric acid.

region to perpendicular to that plane in the asymptotic products. The physical basis for introducing a restricted correlation diagram, one that does not allow such a change, is as follows. For a $^1A'$ state of nitric acid to correlate to an A'' NO_2 product state, the OH fragment must develop A'' symmetry along the reaction coordinate. We propose that in a diabatic representation of the states of nitric acid, the off-diagonal configuration interaction matrix elements that facilitate such a change in the electronic wave function (a change that would allow the molecule to access the light dotted line states in the figure from excitation to the low-lying states of nitric acid) are exceedingly small, even smaller than Woodward–Hoffmann forbidden couplings for electronic changes localized on the NO_2 moiety. For example, the $NO_2(1\,^2A_1)+OH(A'')$ products correlate diabatically to a high-lying excited state of nitric acid corresponding to excitation from the out-of-plane nonbonding orbital on the OH moiety to the σ^* orbital along the N–OH bond.

Thus, in the full correlation diagram of nitric acid, the $1\,^1A''$ excited state correlates adiabatically with ground state NO_2+OH via an avoided crossing where the electronic configuration changes from $\{\ldots(4b_2)^1(3b_1)^1\}$ in the Franck–Condon region to $\{\ldots(2b_1)^1(6a_1)^1\}$ after the avoided crossing en route to products. Due to the considerable electronic rearrangement on the OH fragment required for the molecule to produce $NO_2(1\,^2A_1)+OH$ fragments upon excitation to the $1\,A''$ excited state, the configuration interaction matrix elements are extremely small and this pathway is disallowed in our restricted adiabatic correlation diagram, just as the correlations of the $3\,^1A'$ and $4\,^1A'$ states to $NO_2(1\,^2A_2)$ and $NO_2(1\,^2B_1)$ products are disallowed.

Both the restricted correlation diagram and the molecular orbital correlation diagram reveal a possible electronic state for the nonadiabatic NO_2 product. Since the electronic configuration for the $NO_2(1\,^2B_2)$ fragment is $\{\ldots(4b_2)^1(6a_1)^2\}$, the $OH+NO_2(1\,^2B_2)$ products correlate diabatically to a higher lying $^1A'$ excited state of nitric acid, $4b_2(9a')\rightarrow 6a_1(10a')$, as shown by the orbital correlation diagram. Since this state is the same symmetry as the $2\,^1A'$ excited state, $a_2(3a'')\rightarrow 3b_1(4a'')$, they mix and split to form an avoided crossing along the $OH+NO_2(1\,^2B_2)$ reaction coordinate. As already stated, this reaction is Woodward–Hoffmann forbidden, so that instead of traversing the barrier to products, the electronic wave function may retain the local $\pi_{nb,O}\rightarrow\pi^*_{NO_2}(a_2\rightarrow 3b_1)$ character and undergo a diabatic dissociation. This pathway produces NO_2 in its $2\,^2B_2$ electronic state, not the $1\,^2B_2$ electronic state, since the electronic excitation for the $NO_2(2\,^2B_2)$ product is $1a_2\rightarrow 2b_1$. This nonadiabatic pathway is illustrated in our restricted correlation diagram, Fig. 13, for if the molecule does not follow the adiabatic pathway along the $2\,^1A'$ potential energy surface, but instead undergoes a nonadiabatic transition to the upper $3\,^1A'$ surface, $OH+NO_2(2\,^2B_2)$ products result. Spectral interpretation by Warsop and co-workers,[35] however, determines the electronic energy for this upper $^2B_2$ state as 4.98 eV, which is energetically inaccessible by 14 kcal/mol. Although earlier SCF-CI calculations by Jackels and Davidson[36] calculate the minimum electronic energy as 3.73 eV, two groups have obtained more accurate results to aid in our assignments. Maurice and Head-Gordon[37] use XCIS calculations to determine a vertical excitation energy of 5.03 eV for the $NO_2(2\,^2B_2)$ state. Recent MRCISD calculations by Kedziora *et al.*[38] determine the minimum electronic energy for this state as 5.20 with a DZP basis and 5.48 eV with a TZP basis. Thus, this electronic state is clearly energetically inaccessible and cannot account for the second pathway.

We also present a restricted correlation diagram for the triplet states of nitric acid, Fig. 14. This figure reveals another possible mechanism, rapid spin-orbit coupling to the triplet manifold to produce a low-lying quartet state of NO_2. Two possible candidates are the $1\,^4B_2$ and $1\,^4A_2$ electronic states. Calculations by Jackels and Davidson[36] show minimum energies for the two quartet states as 2.38 and 2.58 eV, respectively. Calculations from quartet XCIS using the NO_2 geometry in ground state nitric acid give a vertical excitation energy of 3.59 for the $1\,^4B_2$ state and 3.72 eV for the $1\,^4A_2$ state.[37] These values predict peak kinetic energies of 18 and 15 kcal/mol, respectively. On the other hand, higher level calculations using third-order perturbation theory and a CC-PVTZ basis[38] with the NO_2 geometry in ground state nitric acid predict a vertical excitation energy of 4.38 eV for the lower-lying $1\,^4B_2$ state. Since this estimate predicts the most probable internal energy for the NO_2 fragments as 101 kcal/mol, the most probable translational energy would occur around zero; therefore, these calculations indicate a quartet state is unlikely. Thus, further calculations, such as the minimum energies for the quartet states, are needed to definitively assign this second electronic state.

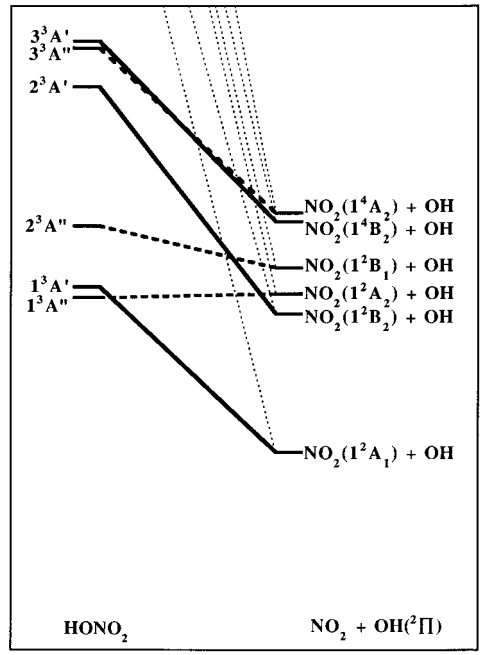

FIG. 14. ''Restricted adiabatic'' state correlation diagram for the triplet states of nitric acid and the $OH+NO_2$ asymptotic products with a NO_2 bend angle of 130°. The vertical excitation energies for the excited states of nitric acid and for the NO_2 electronic states are taken from Ref. 22 and Ref. 37, respectively. The bold dashed and solid lines correlate to products in which the OH radical p electron is restricted to remain symmetric with respect to the parent molecular plane of nitric acid, i.e., a'. The A' states are indicated by the solid lines, whereas the A'' states are indicated by the dashed lines. The avoided crossings that result from the light dotted lines are not drawn because these lines correlate to high-lying excited states of nitric acid with an electron in a σ^*(N–OH) orbital (see Fig. 13 caption). This figure reveals that intersystem crossing to the triplet manifold could result in NO_2 in one of the low-lying quartet states, $1\,^4B_2$ or $1\,^4A_2$.

To provide further support for our proposal that the OH radical electron in nitric acid does not reorient to an orbital perpendicular to the molecular plane, we can examine other systems which undergo $R+NO_2$ dissociation. Both methyl nitrate, CH_3ONO_2, and nitromethane, CH_3NO_2, have low-lying excited states involving transitions localized on the NO_2 moiety analogous to nitric acid.[30] Similarly, two distinct kinetic energy distributions for the $R+NO_2$ channels are measured for CH_3NO_2[39] and CH_3ONO_2[40] upon photodisso-

TABLE II. Observed internal energies of the NO_2 products in $R+NO_2$ dissociation assuming negligible partitioning of internal energy to R.

System	E_{mp}^{int} (fast) (kcal/mol)	E_{mp}^{int} (slow) (kcal/mol)
$HONO_2$	65	86
CH_3ONO_2	67	88
CH_3NO_2	80	86

ciation at 193 nm. Table II compares the most probable internal energies of all three molecules for both $R+NO_2$ channels determined from the kinetic energy distributions. Since the internal energies of the NO_2 fragments from the photodissociation of nitromethane are similar to nitric acid, this system provides compelling evidence for our restricted correlation diagram. Unlike OH, the CH_3 radical is not doubly degenerate; only an a' orbital is available for the lone electron. Thus, the correlation diagram for the low-lying states of CH_3NO_2 is very different from the correlation diagram for $HONO_2$. Our proposed restricted correlation diagram for the low-lying excited states of $HONO_2$, however, is similar to the correlation diagram for CH_3NO_2. In agreement with our assignment of the faster NO_2 fragments, Butler and co-workers[39(a)] assigned the predominant and faster channel in nitromethane to $CH_3+NO_2(1\,^2B_2)$ based on the measured fluorescence excitation spectrum and energetic considerations. They attributed the minor channel, which produces very slow fragments, to $CH_3+NO_2(2\,^2B_2)$ products based on the calculations by Jackels and Davidson.[36] Although we agree with their assignment for the fast CH_3+NO_2 products, calculations by Kedziora *et al.*[38] show the $NO_2(2\,^2B_2)$ is energetically inaccessible. Similar to the OH fragment in nitric acid, the CH_3O fragment produced from the photodissociation of methyl nitrate is doubly degenerate. We propose that the radical p electron for CH_3O also remains in the plane of the parent molecule. Although Huber and co-workers[40] do not definitively assign the CH_3O+NO_2 channels in methyl nitrate, we assign the predominant and faster channel to $CH_3O+NO_2(1\,^2B_2)$.

C. O+HONO channels

We also measured two different kinetic energy distributions for the O+HONO pathway, although only minor branching to the channel at low kinetic energies is observed. This channel was not reported by Huber and co-workers,[3] since they attributed the slow signal at NO_2^+ to clusters. As we suggested earlier, these two channels most likely result from different electronic states of HONO since they possess very different daughter-ion cracking patterns. In order to determine the electronic states for these two channels, we begin by considering two spin-conserving pathways,

$$HNO_3 \rightarrow O(^3P)+HONO(a\ ^3A''), \tag{5}$$

$$HNO_3 \rightarrow O(^1D)+HONO(X\ ^1A'). \tag{6}$$

The translational energy distributions for these channels, Fig. 6, show that the minor O+HONO channel peaks at 1 kcal/mol and extends to approximately 10 kcal/mol, whereas the dominant O+HONO channel peaks around 8 kcal/mol and extends to 25 kcal/mol. To aid in our assignments, we present an adiabatic correlation diagram along the O+HONO reaction coordinate for the singlet excited states for nitric acid.[41] The correlation diagram for the singlet states, Fig. 15, shows that the photoprepared $2\,^1A'$ state correlates adiabatically to $O(^1D)+HONO(X\ ^1A')$, not to the somewhat higher energy channel (0.63 eV higher vertical energy) of triplet $HONO+O(^3P)$.[42] We assign the major channel to $O(^1D)+HONO(X\ ^1A')$ and the minor channel to $O(^3P)+HONO(a\ ^3A'')$.

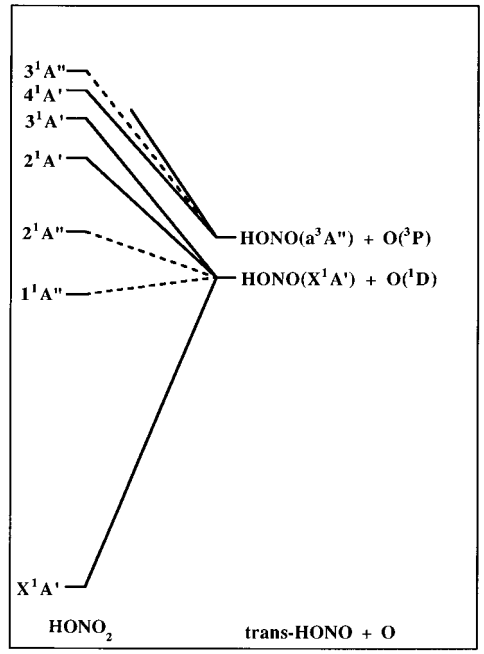

FIG. 15. Fully adiabatic state correlation diagram for the singlet states of nitric acid and the O+HONO asymptotic products. The vertical excitation energies shown for the excited states of nitric acid are taken from Ref. 22. The vertical excitation energies shown for the HONO electronic states, which are calculated using the trans conformer, are taken from Ref. 42. The A' states are indicated by the solid lines, whereas the A'' states are indicated by the dashed lines. The $2\,^1A'$ state, which is accessed at 193 nm, correlates adiabatically to $HONO(X\ ^1A')+O(^1D)$. The unconnected line for the $HONO(a\ ^3A'')+O(^3P)$ products correlates to the higher lying $5\,^1A'$ excited state of nitric acid, which is not shown.

To understand why we observe a minor O+HONO pathway, we examine cuts along the O+HONO reaction coordinate from the *ab initio* configuration interaction with single excitations only calculations.[43] The output from the CIS calculations shows the $2\,^1A'$ state correlates to $O(^3P)+HONO(a\ ^3A'')$, in disagreement with the fully adiabatic correlation diagram in Fig. 15. This is expected since the CI expansion must include excited electronic configurations with double excitations in order for the $2\,^1A'$ excited state to correlate to $O(^1D)+HONO(X\ ^1A')$. Thus, the CIS calculations will not give the fully adiabatic correlations, they will only give the adiabatic channel in the restricted case where only single excitations are allowed. Since the electronic change required for the formation of $O(^1D)+HONO(X\ ^1A')$

is centered on orbitals that are not remote from the electronic transition in nitric acid, this pathway is experimentally observed. The other observed pathway to $O(^3P)+HONO(a\ ^3A'')$ is predicted in the CIS calculation, the equivalent of a restricted adiabatic correlation if one only allows single electronic changes in orbital occupancies along the reaction coordinate. This observed pathway would then compare to a nonadiabatic hop to an upper adiabat, such as the $4\ ^1A'$ excited state in nitric acid in the full adiabatic correlation diagram.

D. Quantum yield measurements

The final goal in this paper is to resolve the discrepancies of the quantum yield measurements from the photodissociation of nitric acid at 193 nm. Our branching ratio, which includes the minor O+HONO pathway, is $(OH+NO_2)/(O+HONO)=0.50\pm0.05$. In order to compare our branching ratios with the quantum yield measurements, we convert our ratio into product yields. Since the photodissociation occurs on a time scale faster than fluorescence, as illustrated by the anisotropic angular distributions, the branching ratio can be directly converted into quantum yields since fluorescence is a negligible competing process. We obtain $\Phi(OH)=0.33\pm0.04$ and $\Phi(O_{total})=0.67\pm0.04$. In the introduction, we reviewed two conflicting spectroscopic measurements of the OH quantum yield. Our OH quantum yield agrees with the quantum yield reported by Ravishankara and co-workers[1] $[\Phi(OH)=0.33\pm0.06]$ and is smaller than the OH quantum yield reported by Schiffman and Nesbitt[2] $[\Phi(OH)=0.47\pm0.06]$. Our OH quantum yield is also out of range of the value reported by prior photofragment velocity analysis molecular beam studies by Huber and co-workers[3] $[\Phi(OH)=0.6\pm0.1]$, who relied on a daughter-ion cracking pattern of HONO, which did not include fragmentation to O^+ in the ionizer. Ravishankara and co-workers also measured $\Phi(O_{total})=0.81\pm0.13$, which is higher than our measurement because it includes contributions from the secondary dissociation of NO_2. Our primary $O(^1D)$ quantum yield of $\Phi(O^1D)=0.54\pm0.04$ differs from the value of $\Phi O(^1D)=0.28\pm0.07$ reported by Ravishankara and co-workers.

V. SUMMARY

In this paper, we introduce a new method for generating a restricted adiabatic correlation diagram to identify which adiabatic and nonadiabatic product channels are likely to occur upon photoexcitation. The restricted correlation diagram, which does not allow large changes in the electronic character on remote portions of the molecule along the reaction coordinate, can be applied to other systems as long as the transition is localized on a functional group in the molecule. We plan to investigate a variety of systems in order to further develop this concept.

ACKNOWLEDGMENTS

This work was supported by the National Science Foundation, currently under renewal Grant No. CHE-9619376. T.L.M. acknowledges support from an Environmental Protection Agency fellowship, and N.R.F. acknowledges support from the Natural Sciences and Engineering Research Council of Canada for a 1967 Science and Engineering Scholarship. We would also like to acknowledge two groups, (1) M. Head-Gordon and D. R. Maurice at the University of California at Berkeley, and (2) Al Wagner, Ron Shepard, Larry Harding, and Gary Kedziora at Argonne National Laboratory, for taking an interest in calculating the electronic states of NO_2 and communicating their results prior to publication. We also thank Charles Miller for providing us with both published and unpublished results on nitric acid.

[1] A. A. Turnipseed, G. L. Vaghijiani, J. E. Thompson, and A. R. Ravishankara, J. Chem. Phys. **96**, 5887 (1992).
[2] A. Schiffman, D. D. Nelson, Jr., and D. J. Nesbitt, J. Chem. Phys. **98**, 6935 (1993).
[3] P. Felder, X. Yang, and J. R. Huber, Chem. Phys. Lett. **215**, 221 (1993).
[4] F. Biaume, J. Photochem. **2**, 139 (1973).
[5] H. S. Johnston, S.-G. Chang, and G. Whitten, J. Phys. Chem. **78**, 1 (1974).
[6] J. August, M. Brouard, and J. P. Simons, J. Chem. Soc. Faraday Trans. 2, **84**, 587 (1988); M. Brouard, S. Duxon, P. A. Enriquez, and J. P. Simons, J. Chem. Soc. Faraday Trans. **89**, 1435 (1993).
[7] A. Sinha, R. L. Vander Wal, and F. F. Crim, J. Chem. Phys. **91**, 7436 (1989).
[8] A. Sinha, R. L. Vander Wal, L. J. Butler, and F. F. Crim, J. Phys. Chem. **91**, 4645 (1987).
[9] J. August, M. Brouard, M. P. Docker, H. Hodgson, C. J. Milne, and J. P. Simons, Ber. Bunsenges. Phys. Chem. **92**, 264 (1988).
[10] C. E. Miller and H. S. Johnston, J. Phys. Chem. **97**, 9924 (1993).
[11] G. Hancock (private communication).
[12] Y. Y. Bai and G. A. Segal, J. Chem. Phys. **92**, 7479 (1990).
[13] The prior assignments for the excited states of NO_2 use the plane of the molecule as the *yz* plane so that b_1 is antisymmetric with respect to the reflection in the molecular plane and b_2 is symmetric with respect to reflection in the molecular plane. Although Bai and Segal use this standard for assigning their symmetries, they incorrectly refer to the $NO_2(1\ ^2B_2)$ state as linear.
[14] M. Suto and L. C. Lee, J. Chem. Phys. **81**, 1294 (1984).
[15] R. Kenner, F. Rohrer, T. Papenbrock, and F. Stuhl, J. Phys. Chem. **90**, 1294 (1986).
[16] Y. T. Lee, J. D. McDonald, P. R. LeBreton, and D. R. Herschbach, Rev. Sci. Instrum. **40**, 1402 (1969).
[17] M. D. Person, Ph.D. thesis, Department of Chemistry, University of Chicago, 1991.
[18] E. W. Washburn, *International Critical Tables of Numerical Data, Physics, Chemistry, and Technology*, 1st ed. (McGraw-Hill, New York, 1926), Vol. III, p. 305.
[19] Very different daughter-ion cracking patterns were observed for ground state and electronically excited HOCO radicals. See D. C. Kitchen, N. R. Forde, and L. J. Butler, J. Phys. Chem. **101** (in press) (1997).
[20] P.-S. Yeh, G.-H. Leu, Y.-P. Lee, and I-C. Chen, J. Chem. Phys. **103**, 4879 (1995).
[21] R. N. Zare, Mol. Photochem. **4**, 1 (1972).
[22] A. M. Graña, T. J. Lee, and M. Head-Gordon, J. Phys. Chem. **99**, 3493 (1995).
[23] We estimated the ionization cross sections using the empirical relationship obtained in R. E. Center and A. Mandl, J. Chem. Phys. **57**, 4104 (1972), $\sigma_{ion}(10^{-16}\ \text{Å}^2)=36(\alpha^{1/2})-18$. The atomic polarizability, α, of 0.802 Å^3 for O and 0.666 793 Å^3 for H is given in T. M. Miller and B. Bederson, Adv. At. Mol. Phys. **13**, 1 (1977). The molecular polarizability of 1.469 Å^3 for OH is calculated by summing the atomic polarizabilities of O and H.
[24] G. D. Gillispie, A. U. Khan, A. C. Wahl, R. P. Hosteny, and M. Krauss, J. Chem. Phys. **63**, 3425 (1975).
[25] A. Jacobs, K. Kleinermanns, H. Kuge, and J. Wolfrum, J. Chem. Phys. **79**, 3162 (1983).
[26] G.-H. Leu, C.-W. Hwang, and I-C. Chen, Chem. Phys. Lett. (submitted).

[27] H. Katagiri and S. Kato, J. Chem. Phys. **99**, 8805 (1993). The curves have a fixed NO bond length of 1.193 Å.
[28] G. Hirsch and R. J. Buenker, Can. J. Chem. **63**, 1542 (1984).
[29] See, for example, extensive references cited in M. Hunter, S. A. Reid, D. C. Robie, and H. Reisler, J. Chem. Phys. **99**, 1083 (1993).
[30] L. E. Harris, J. Chem. Phys. **58**, 5615 (1973).
[31] P. E. Cade and W. M. Huo, J. Chem. Phys. **47**, 614 (1967).
[32] C. R. Brundle, D. Neumann, W. C. Price, D. Evans, and D. G. Streets, J. Chem. Phys. **53**, 705 (1970).
[33] W. H. Fink, J. Chem. Phys. **49**, 5054 (1968).
[34] G. C. G. Waschewsky, P. W. Kash, T. L. Myers, D. C. Kitchen, and L. J. Butler, J. Chem. Soc. Faraday Trans. **90**, 1581 (1994).
[35] R. K. Ritchie, A. D. Walsh, and P. A. Warsop, Proc. R. Soc. London Ser. A **266**, 257 (1962).
[36] C. F. Jackels and E. R. Davidson, J. Chem. Phys. **65**, 2941 (1976).
[37] D. R. Maurice and M. Head-Gordon (private communication).
[38] G. Kedziora, L. Harding, A. Wagner, and R. Shepard (private communication).
[39] (a) K. Q. Lao, E. Jensen, P. W. Kash, and L. J. Butler, J. Chem. Phys. **93**, 3958 (1990); (b) L. J. Butler, D. Krajnovich, Y. T. Lee, G. Ondrey, and R. Bersohn, *ibid.* **79**, 1708 (1983).
[40] X. Yang, P. Felder, and J. R. Huber, J. Phys. Chem. **97**, 10,903 (1993).
[41] To generate the correlation diagram for the O+HONO channels, we followed examples of correlation diagrams for a similar system, the photodissociation of ozone to O_2+O. See A. Banichevich and S. D. Peyerimhoff, Chem. Phys. **178**, 155 (1993).
[42] C. Larrieu, A. Dargelos, and M. Chaillet, Chem. Phys. Lett. **91**, 465 (1982).
[43] These calculations were performed using GAUSSIAN 92. See GAUSSIAN 92, Revision C, M. J. Frisch, G. W. Trucks, M. Head-Gordon, P. M. W. Gill, M. W. Wong, J. B. Foresman, B. G. Johnson, H. B. Schlegel, M. A. Robb, E. S. Replogle, R. Gomperts, J. L. Andres, K. Raghavachari, J. S. Binkley, C. Gonzalez, R. L. Martin, D. J. Fox, D. J. Defrees, J. Baker, J. J. P. Stewart, and J. A. Pople, Gaussian, Inc., Pittsburgh, PA, 1992.